UV-Supercontinuum generated by femtosecond pulse filamentation in air: Meter-range experiments versus numerical simulations

G. Méjean,[1] J. Kasparian,[1] J. Yu,[1] S. Frey,[1] E. Salmon,[1]

R. Ackermann,[1] J.P. Wolf,[1] L. Bergé,[2] and S. Skupin[2,3]

[1] *Laboratoire de Spectrométrie Ionique et Moléculaire,*

Université Cl. Bernard Lyon 1, UMR-CNRS 5579,

F-69622 Villeurbanne cedex, Lyon, France.

[2]*Département de Physique Théorique et Appliquée,*

CEA/DAM Ile de France, B.P. 12, 91680 Bruyères-le-Châtel, France.

[3] *Friedrich-Schiller-Universität Jena,*

Max-Wien-Platz 1, 07743 Jena, Germany.

(Dated: October 25, 2005)

Abstract

We report new experimental and numerical results on supercontinuum generation at ultraviolet/visible wavelengths produced by the propagation of infrared femtosecond laser pulses in air. Spectral broadening is shown to affect similarly single filaments over laboratory scales as well as broad beams over long-range propagation distances. Numerical simulations display evidence of the crucial role of third harmonic generation in the build-up of UV-visible wavelengths, by comparison with current single-envelope models including chromatic dispersion and self-steepening.

PACS numbers: 52.38.Hb, 42.65.Tg, 42.65.Jx, 42.68.Ay

While propagating in air, ultrashort laser pulses undergo filamentation [1] due to the dynamic interplay between Kerr focusing and self-induced plasma defocusing. Depending on the beam power, this subtle balance generates light filaments, which can develop over several hundreds of meters [2] and even kilometers in the vertical direction [3]. Associated with this property, the temporal variations experienced by the pulse produce a very broad spectral continuum, spanning from UV to IR wavelengths. Coherence is preserved between the different spectral components, so that the broadened pulse is often referred to as a "white light laser" [4]. Part of this supercontinuum leaks out from the beam as a narrow cone in the forward direction, called "conical emission" [5], with typical half-angle of $\sim 0.12°$ at 0.5 μm.

Most experimental and theoretical investigations using femtosecond Ti:Sa laser sources (0.8 μm) reported spectral broadening extending from 4.5 μm to an UV cut-off around 0.35 μm [6]. However, a few years ago pioneering results demonstrated that another emission peak around 0.27 μm arises from an additional process: Third Harmonic Generation (THG) [7, 8]. Although these studies were limited to low energies (few mJ) and short propagation distances (tens of cm), THG conversion efficiencies as high as 0.2 % were measured. More recently, a couple of publications appeared in this field [9, 10]. In Ref. [9], supercontinuum generation (SCG) extending up to 0.23 μm in air was experimentally observed over laboratory scales. As the beam energy was increased from 250 μJ to 10 mJ, TH spectrum was seen to merge into the blue side of the supercontinuum generated by the IR pump, resulting in a continuous broad spectral band in the UV-visible wavelength domain. Frequency variations of the TH component, mainly dictated by cross-phase modulation induced by the pump, were expected to produce this effect, to the detriment of self-steepening and chromatic dispersion. In Ref. [10], the same phenomenon of UV-visible SCG in air was reported over much longer distances ($\sim$ 200 m), by means of Light Detection and Ranging (Lidar) experimental setup. From the theoretical point of view, numerical simulations evidenced the following properties: (i) UV-visible spectral broadening is created by the overlap of redshift from the TH component and blueshift from the IR pump. Frequency shifts depend on the component phases (ϕ_j, $j = \omega, 3\omega$), such as $\Delta\omega_j = -\partial_t\phi_j$, subject to the phase-locking constraint $\Delta\phi = 3\phi_\omega - \phi_{3\omega} \simeq \pi$ in filamentation regime (see also [7]). (ii) The TH component behaves as a weak quintic-type defocusing nonlinearity on the fundamental dynamics: This saturation lowers the maximum intensity of the IR component and significantly increases the filament

range by ~ 1 m. (iii) TH-induced saturation superimposes with plasma generation to defocus the pulse and enlarge the conical emission to $\sim 0.25°$ at 0.25 μm.

In spite of these investigations, two questions remain open. First, numerical limitations prevented realistic simulations of broad beams [10] from accessing Lidar propagation ranges. Although differences between meter-range simulations and Lidar data (≥ 100 m) occurred in the longitudinal scales, the spectral dynamics, however, looked similar, which received no explanation. Second, the role of chromatic dispersion and self-steepening compared with THG remains unclear. Whereas the former processes are capable of enlarging the fundamental spectrum to the UV regions [11, 12], their relative strength compared with THG deserves a special investigation.

Therefore, the issues addressed in this paper are twofold: First, because a direct comparison between spectral dynamics on laboratory scales and over Lidar ranges is missing, we experimentally demonstrate that filaments lead to analogous supercontinua in long-range Lidar propagation as well as in laboratory-scaled experiments. Emphasis is next given to the spectral distortions developing *along meter-range distances* from the second experimental setup as well as in numerical computations. We investigate this spectral dynamics by means of two models, one involving THG without self-steepening and chromatic dispersion, the other one describing the pump wave including these effects. THG equations are shown to yield more accurate results than the latter model.

Range resolved spectra have been measured using two different setups. For long scales, the Teramobile laser system [13] was arranged in a Lidar-based configuration, delivering 10-Hz rated, 5 TW pulses (70 fs, 350 mJ) centered at 0.8 μm. A beam with 10 cm diameter was sent vertically into the atmosphere. The Rayleigh-Mie scattering signals were inverted with standard algorithms [14]. Chirp and beam focusing produced pulse duration of 150 fs and 10 m focal length, which optimized white-light generation at long distances. Spectra were measured with 10 nm resolution from 0.23 μm to 0.6 μm, for 10-m range resolution along the optical path (see [10] for more details). On the other hand, meter-scale experiments were performed with a Ti:Sa CPA laser system providing ~ 60 GW pulses (9 mJ, ~ 150 fs) centered at 0.81 μm. The 12 mm diameter beam freely propagated over 6.1 m and was focused with a $f = 5$ m convergent mirror, so as to produce a single filament at a distance of about 3.3 m from the mirror. The UV-visible part of the supercontinuum, reflected from the edge of a glass plate set nearby the filament, was measured with a photomultiplier tube

attached to a monochromator, providing 7 nm spectral resolution. We checked carefully that no white light was generated in the glass plate. Each point of the spectra was integrated over 128 laser shots.
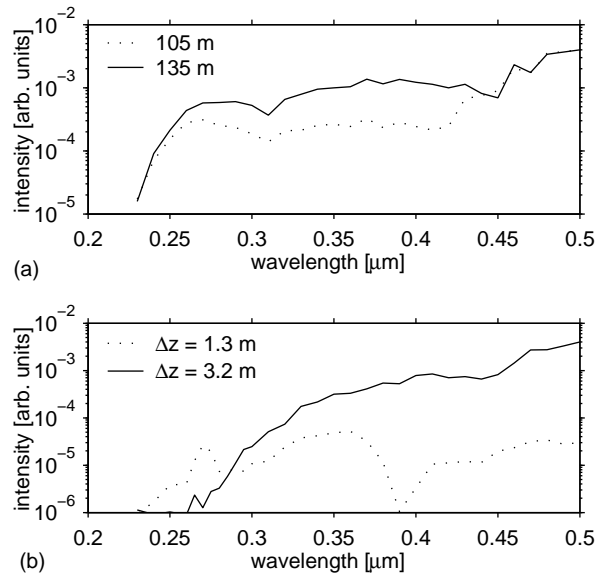

(a)

(b)

FIG. 1: Spectra in the wavelength domain $0.2 \leq \lambda \leq 0.5$ μm for different propagation distances. (a) Spectra developing over 135 m measured by Lidar arrangement [10]; (b) Experimental data from laboratory measurements. In 1(b), Δz is the longitudinal distance from the nonlinear focus $z_c \simeq 3.3$ m (filament onset distance). Spectral intensity at 0.5 μm is fixed to 4×10^{-3} times that of the fundamental [6], except for $\Delta z = 1.3$ m where its value is two decades below (3×10^{-5}).

The spectral evolution resulting from the first setup is recalled from Ref. [10] in Figure 1(a). At 105 m, a 50 nm broad THG band appears around 0.27 μm. From 135 m, the spectrum changes into an ultrabroad, continuous UV-visible plateau, which forms a hump in the wavelength domain $0.27 \leq \lambda \leq 0.5$ μm. This hump persists at longer distances, whereas UV components become more depleted (see Fig. 6 of Ref. [10]). As shown in Fig. 1(b), the same behavior develops over much shorter distances from a single filament created with the second experimental setup. At short distances close to the nonlinear focus (filamentation onset distance, noted $z_c \simeq 3.3$ m), SPM widely broadens the pump spectrum. At $\Delta z = z - z_c \simeq 1.3$ m from the focus, a 20 nm THG band appears around 0.27 μm. This spectral enlargement is comparable with that detected in laboratory [8] over some tens of cm and more recently in [9] by increasing the beam energy. About 2 m later ($\Delta z \simeq 3.2$

m), THG is depleted and a continuous UV-visible plateau appears, creating a hump in the 0.3-0.5 μm region. At further distances, this plateau was observed to hold its shape, far beyond the end of the filament.

Figs. 1(a) and 1(b) exhibit the same spectral dynamics. Major changes, however, occur over longer distances in the Lidar configuration, because multifilamentation takes place in the Teramobile bundle that conveys high (TW) powers. The fact that long-range Lidar propagation and laboratory-scaled experiments develop comparable SCG can be explained by the generic dynamics of a single filament. Differences in the longitudinal scales are explained as follows. In Fig. 1(a), the broad TW beam breaks up into multiple filaments, each having a typical length of $\sim$ 1 m and individual power of $\sim$ 10 GW [15]. The Lidar beam then consists of the incoherent superposition of $\sim$ 100 independent filaments, randomly nucleated along the propagation axis. The build-up in wavelengths arises over longer intervals in this configuration ($\Delta z \sim$ 30 m), because most filaments are not aligned on the same Fourier profile in the early filamentation stage. Reaching a quasi-coherent state consumes several tens of meters along the optical path, in order to modify the total spectrum noticeably. The similarity in the spectral shapes of Fig. 1 confirms these properties and, thereby, raises the conjecture stated in Ref. [10].

To reproduce this spectral dynamics, we performed numerical simulations using the model equations of Ref. [10], which couple the slowly-varying envelopes of the fundamental wave ($\mathcal{E}_\omega$) with the TH one ($\mathcal{E}_{3\omega}$) as

$$\frac{\partial \mathcal{E}_j}{\partial z} = \left(i\beta_j \nabla_\perp^2 - \alpha_j \frac{\partial}{\partial t} - i\frac{k_j''}{2}\frac{\partial^2}{\partial t^2} - i\delta_j \right) \mathcal{E}_j + \mathcal{F}_j + \mathcal{P}_j, \tag{1}$$

where $j = \omega, 3\omega$. In Eq. (1), z is the propagation variable, t is the time coordinate retarded in the pump frame, and $\nabla_\perp^2 = r^{-1}\partial_r r \partial_r$; $\alpha_{3\omega} = \Delta v^{-1}$, where $\Delta v = [v_g(3\omega)^{-1} - v_g(\omega)^{-1}]^{-1} = $ 0.44 cm/fs is the group-velocity mismatch responsible for temporal walk-off ($\alpha_\omega = 0$), $\beta_{3\omega} = \beta_\omega/3 = 1/6k_0$ with $k_0 = 2\pi/\lambda_\omega$; $k_\omega'' = 0.2$ fs^2/cm and $k_{3\omega}'' = 1$ fs^2/cm are the coefficients for group-velocity dispersion (GVD) and $\delta_{3\omega} = \Delta k \equiv 3k(\omega) - k(3\omega) = -5$ cm^{-1} is the wave vector mismatch ($\delta_\omega = 0$). The function $\mathcal{F}_j$ represents the optical nonlinearities, involving

5

self-, cross-phase modulations and four-wave mixing:

$$\mathcal{F}_\omega = ik_0 n_2 \left(R(t)\mathcal{E}_\omega + 2|\mathcal{E}_{3\omega}|^2\mathcal{E}_\omega + \mathcal{E}_\omega^{*2}\mathcal{E}_{3\omega} \right) \tag{2}$$

$$\mathcal{F}_{3\omega} = ik_0 n_2 \left(3\frac{n_2^{3\omega}}{n_2}|\mathcal{E}_{3\omega}|^2\mathcal{E}_{3\omega} + 6|\mathcal{E}_\omega|^2\mathcal{E}_{3\omega} + \mathcal{E}_\omega^3 \right) \tag{3}$$

$$R(t) = \frac{1}{2}|\mathcal{E}_\omega|^2 + \frac{\tau_K^{-1}}{2}\int_{-\infty}^{t} e^{-(t-t')/\tau_K}|\mathcal{E}_\omega(t')|^2 dt. \tag{4}$$

The function $\mathcal{P}_j$ describes the plasma response with free electron density ρ as

$$\mathcal{P}_j = -i\frac{\beta_j k_0^2}{\rho_c}\rho\mathcal{E}_j - \frac{\sigma_j}{2}\rho\mathcal{E}_j - \frac{\beta_j^{(K_j)}}{2}|\mathcal{E}_j|^{2K_j-2}\mathcal{E}_j \tag{5}$$

$$\frac{\partial\rho}{\partial t} = \sum_{j=\omega,3\omega}(\rho_{\rm nt} - \rho)\sigma_{(K_j)}|\mathcal{E}_j|^{2K_j} + \frac{\sigma_j}{U_i}\rho|\mathcal{E}_j|^2, \tag{6}$$

where K_j, $\sigma_{(K_j)}$ and $\beta_j^{(K_j)}$ denote the number of photons for IR and UV wavelengths, multiphoton ionization rates and related absorption losses for dioxygen molecules, respectively. Plasma response includes avalanche ionization with cross-sections σ_j. Eqs. (1-6), whose values of the physical parameters can be found in Ref. [10], were numerically integrated in radial symmetry to compute the spectra emitted by a single filament at the propagation distances experimentally scanned in Fig. 1(b).

For comparison, we also performed computations of the ω component alone, undergoing self-steepening and chromatic dispersion. These effects being responsible for a strong blue-shift of fs spectra in air [11, 12], they may possibly inhibit the influence of THG and cause by themselves UV-visible SCG. In that case, the envelope $\mathcal{E}_\omega$ is governed by the equation:

$$\frac{\partial\mathcal{E}_\omega}{\partial z} = \frac{i}{2k_0}T^{-1}\nabla_\perp^2\mathcal{E}_\omega + i\hat{D}\mathcal{E}_\omega - \frac{ik_0}{2\rho_c}T^{-1}\rho\mathcal{E}_\omega - \frac{\sigma_\omega}{2}\rho\mathcal{E}_\omega$$
$$+ ik_0 n_2 T R(t)\mathcal{E}_\omega - \frac{\beta^{(K_\omega)}}{2}|\mathcal{E}_\omega|^{2K-2}\mathcal{E}_\omega, \tag{7}$$

where ρ obeys Eq. (6) for the IR pulse parameters chosen above. $\hat{D} = \sum_{n=2}^{5}(k^{(n)}/n!)(i\partial_t)^n$ is the dispersion operator, with coefficients $k^{(n)} \equiv \partial^n k/\partial\omega^n|_{\omega=\omega_0}$ computed from the Sellmeier formula for air ($k''' = 0.1$ fs^3/cm) established in Ref. [16]. This model moreover accounts for space-time focusing ($T^{-1}\nabla_\perp^2\mathcal{E}$) and self-steepening ($T|\mathcal{E}|^2\mathcal{E}$), where $T \equiv 1 + (i/\omega_0)\partial_t$ [17].

With Eqs. (1-6) we simulated one filament starting from a Gaussian pulse with waist $w_0 = 0.5$ mm, FWHM duration of 150 fs and power $P_{\rm in} \simeq 10$ GW. Figure 2(a) shows its spectral evolution at different distances after the nonlinear focus $z_c \simeq 0.4$ m. The plotted

quantity is the normalized spectral intensity integrated in space versus the distance Δz from z_c. Self-focusing first induces SPM in the fundamental pulse. At $\Delta z = 1.3$ m, the TH component broadens in turn around 0.27 μm and experiences a significant "redshift". At $\Delta z \geq 3$ m, the spectrum is increased by about one decade at visible wavelengths, while UV components become more attenuated. Spectral distortions similar to Fig. 1(b) develop over comparable distances shifted from the self-focus point, $\Delta z = z - z_c$. They agree with the experimental data, apart from oscillations created by interferences between different peaks appearing in the pulse profile. Such oscillations are smoothed in the experimental spectra, measured with a resolution of 7 nm and averaged over 128 shots. Some differences, however, exist before the hump in wavelengths fully develops: At $\Delta z = 1.3$ m, the dip located at ~ 0.39 μm in the experimental spectrum is shifted back to 0.32 μm in its numerical counterpart, and the spectral intensity at UV wavelengths fluctuates within one decade. In spite of these minor discrepancies, which we attribute to limitations of radial simulations vs the experimental pulse shape, our numerical results offer a rather good agreement with meter-range experiments. They also reproduce the long-distance spectral behavior recalled in Fig. 1(a), as already noticed in [10].
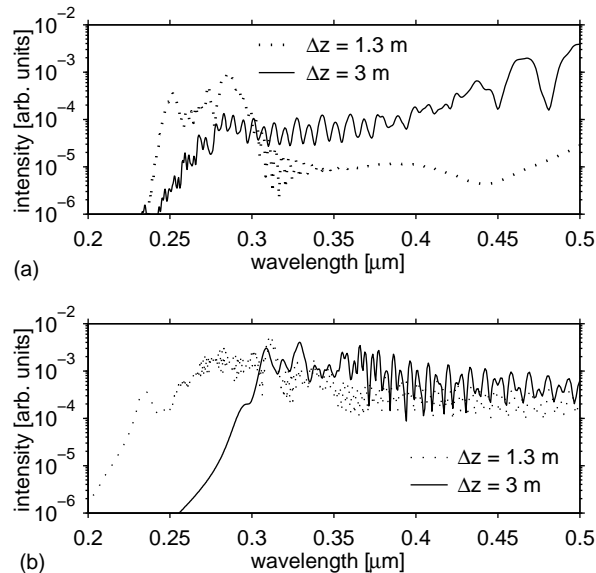

FIG. 2: Spectra numerically computed from (a) Eqs. (1-6) and (b) Eq. (7) vs. intervals Δz from the focus $z_c = 0.4$ m.

Figure 2(b) shows the same pieces of information computed from Eq. (7). A strong extent

of the generated white light develops towards the blue side of the spectra and saturates around 0.2 μm, in agreement with former theoretical predictions [12]. However, simulated at the same intervals Δz, the spectral dynamics changes significantly, compared with Figs. 1(a) and 2(a). The first discrepancy concerns the early spectral broadening of the generated TH, which cannot be described by the single-wave equation (7). While the lower bound of the measured spectra yields the UV cut-off $\lambda_{c.o.} \simeq 0.23$ μm, the continuum computed from Eq. (7) clearly penetrates the far-UV regions < 0.2 μm. The second discrepancy lies in the build-up of wavelengths: Whereas THG forms a plateau of wavelengths *dramatically increasing in intensity* from 0.25 μm to 0.5 μm, the opposite characterizes the spectral dynamics computed from the model (7), i.e., the strong blue-shift created by self-steepening hardly changes in intensity from low to larger wavelengths and remains one decade below the experimental value of the intensity measured at 0.5 μm. As a result, the model equations (1-6) accounting for THG offers a better description of white-light emission and SCG than Eq. (7).

Finally, we briefly compare the temporal pulse profiles of the pump pulse governed by the two models (we remind that TH distributions in time follow the fundamental ones, as shown in [7, 10]). Figure 3(a) shows three characteristic stages in the pulse evolution, linked to the spectral broadenings plotted in Fig. 2(a). We observe that the pump intensity (I_ω) exceeds 2×10^{13} W/cm^2, which agrees with the threshold given in [8]. First a leading peak with sharp edge arises, which asymmetrically broadens the spectra with an early redshift in both components ($\Delta z = 0.9$ m). The pulse is then recentered near $t = 0$ with smoother temporal gradients, which relaxes the spectrum to the blue side ($\Delta z = 1.3$ m). A last focusing event enables the merging of both spectral components from $\Delta z = 3$ m. Figure 3(b) shows temporal profiles computed from the model (7) at analogous distances. Here, the pulse undergoes a shock dynamics within a sharp trailing edge caused by self-steepening [18]. This dynamics produces the spectral extent of the fundamental towards the lowest UV regions, up to $\Delta z = 1.3$ m (see also [11] on this point). This extent diminishes more and more, as the pulse spreads out and smoothes its distribution in time ($\Delta z = 3$ m). The temporal distortions plotted in Fig. 3 thus justify the different spectral dynamics promoted by the numerical models (1) and (7).
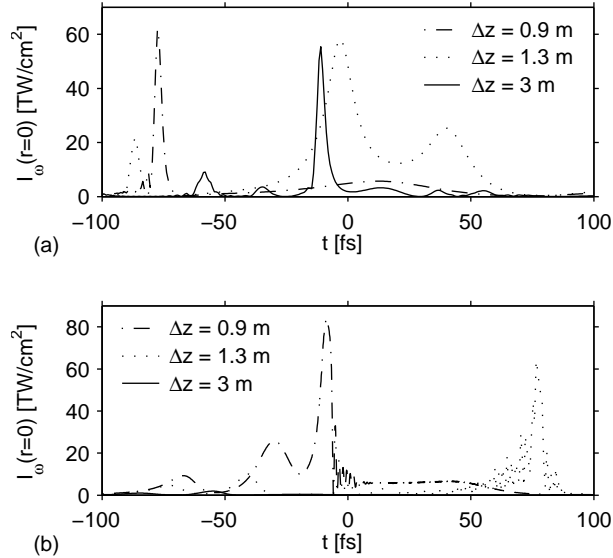
FIG. 3: Temporal profiles at $\Delta z = 0.9$ m (dash-dotted curves), at $\Delta z = 1.3$ m (dotted curves) and $\Delta z = 3$ m (solid curves) for (a) the model accounting for THG without self-steepening and chromatic dispersion [Eq. (1)]; (b) Temporal profiles computed from Eq. (7) at the same distances.

In conclusion, we have shown that the propagation of femtosecond pulses in air is strongly influenced by the nonlinear dynamics of the third harmonic component. Coupling between the pump field and TH develops an important spectral broadening in the wavelength domain $0.23 \leq \lambda \leq 0.5$ μm, which favors supercontinuum generation. Spectral dynamics is identical over meter-range scales as well as over ~ 100 m and beyond. THG dominates over chromatic dispersion and self-steepening in the build-up of wavelengths. This property was evidenced by direct simulations, which showed that including THG improves the qualitative agreement of the numerical results with experiments. Although the focus of this paper mostly concerned results and simulations at meter-range distances, we recalled for the reader's benefit Lidar spectra over more than 100 m [Fig. 1(a)], showing modest changes in the general spectral shapes. Even if we were not able to simulate realistic broad beams so far away, reproducing reasonable agreement upon meter-scale distances make us fairly confident that the physics involved in SCG is mainly captured by the model equation (1).

[1] A. Braun *et al.*, *Opt. Lett.* **20**, 73 (1995).

[2] B. LaFontaine *et al.*, *Phys. Plasmas* **6**, 1615 (1999).

[3] M. Rodriguez *et al.*, *Phys. Rev. E* **69**, 036607 (2004).

[4] S.L. Chin, S. Petit, F. Borne, and K. Miyazaki, *Japan. Journal of Appl. Phys.* **38**, L126 (1999).

[5] O. Kosareva, V.P. Kandidov, A. Brodeur, C.Y. Chien, and S.L. Chin, *Opt. Lett.* **22**, 1332 (1997).

[6] J. Kasparian *et al.*, *Opt. Lett.* **25**, 1397 (2000).

[7] N. Aközbek *et al.*, *Phys. Rev. Lett.* **89**, 143901 (2002).

[8] H. Yang *et al.*, *Phys. Rev. E* **67**, 015401 (2003).

[9] F. Théberge, W. Liu, Q. Luo, and S.L. Chin, *Appl. Phys. B: Lasers and Optics* **80**, 221 (2005).

[10] L. Bergé *et al.*, *Phys. Rev. E* **71**, 016602 (2005).

[11] N. Aközbek, M. Scalora, C.M. Bowden, and S.L. Chin, *Opt. Commun.* **191**, 353 (2001).

[12] M. Kolesik, G. Katona, J.V. Moloney, and E.M. Wright, *Appl. Phys. B: Lasers and Optics* **77**, 185 (2003).

[13] H. Wille *et al.*, *Eur. Phys. Jour. - Applied Physics* **20**, 183 (2002).

[14] R. M. Measures, *"Laser remote sensing - Fundamentals and applications"*, Wiley Interscience, New York (1984).

[15] L. Bergé *et al.*, *Phys. Rev. Lett.* **92**, 225002 (2004).

[16] E. R. Peck and K. Reeder, *J. Opt. Soc. Am.* **62**, 958 (1972).

[17] T. Brabec and F, Krausz, *Phys. Rev. Lett.* **78**, 3282 (1997).

[18] G.P. Agrawal, *"Nonlinear Fiber Optics"*, 3rd Edition, Academic Press, pp. 274 (2001).